



Lean methane flame stability in a premixed generic swirl burner: Isothermal flow and atmospheric combustion characterization

Jon Runyon^{a,*}, Richard Marsh^a, Philip Bowen^a, Daniel Pugh^a, Anthony Giles^a, Steven Morris^b

^a School of Engineering, Cardiff University, Cardiff, Wales, UK

^b Gas Turbine Research Centre, Cardiff University, Margam, Wales, UK

ARTICLE INFO

Keywords:

Turbulent premixed combustion
Generic swirl burner
Lean blowoff
Flame dynamics
Optical diagnostics

ABSTRACT

Gas turbine combustors operating in lean premixed mode are known to be susceptible to flame blowoff due to competing influences of increasing chemical timescales and decreasing flow time scales under these conditions. In this study, combustion stability and the onset of flame blowoff in particular, are characterized in a new swirl burner operated with fully premixed methane (CH₄) and air at thermal power of 55 kW, atmospheric combustor inlet pressure, and ambient (~290 K) combustor inlet temperature. The onset of flame blowoff was shown repeatedly to exhibit high amplitude, low frequency combustion instabilities as a result of periodic flame extinction and reignition events. In addition to detailed isothermal characterization of the burner velocity field using particle image velocimetry, a combination of dynamic pressure sensing and optical combustion diagnostics, including OH* chemiluminescence and OH planar laser induced fluorescence, give indication of the combustion rig acoustic response and changes in flame acoustic response, heat release, and flame anchoring location related to the onset and occurrence of blowoff. This analysis shows that the onset of this instability was preceded by a marked reduction in dominant frequency and amplitude until frequency collapse and high amplitudes were observed throughout the burner inlet mixing plenum, burner pilot, combustion chamber, and exhaust ducting. Acoustic and optical signal analysis show potential viability for use in practical applications for precursor indications of lean blowoff. The flame anchoring location within the combustion chamber was shown to detach from the burner exit nozzle and stabilize within the outer and central recirculation zones near the lean blowoff limit, providing evidence of changes to both chemical and flow time scales. Chemical kinetic modelling is used in support of the empirical studies, in particular highlighting the relationship between maximum heat release rate and OH* chemiluminescence intensity.

1. Introduction

With ever-increasing regulatory pressure on gas turbine manufacturers and operators to reduce NO_x and CO emissions while maintaining high cycle efficiency, combustion systems for land-based power generation have progressed significantly in recent years towards lean premixed (LPM) modes of operation [1]. While delivering emissions reduction benefits, LPM gas turbine combustors are inherently susceptible to potentially high amplitude, low frequency pressure fluctuations associated with operation near the stability limit of lean flame blowoff [2], resulting in potential structural damage to combustion system components, part-load engine operation, or machine shutdown [3]. This phenomenon results from increasing chemical timescales, τ_{chem} , and decreasing flow timescales, τ_{flow} , which can manifest within the combustion chamber as periodic flame extinction and reignition events [4].

While combustion instabilities can be generally categorized as low frequency ($f < \sim 50$ Hz), mid-frequency (~ 50 Hz $< f < \sim 1000$ Hz), and high frequency ($f > \sim 1000$ Hz) [1], the particular lean blowoff (LBO) instabilities observed and characterized in this work fall within the low frequency range. These low frequency instabilities have been noted to occur in both laboratory scale burners [2,4–7] and industrial gas turbine engines [8,9] under operating conditions near LBO. Muruganandam et al. [4] utilized OH* chemiluminescence and acoustic measurements to report that the energy content of the low frequency spectrum (10,200 Hz) increased significantly near LBO at an equivalence ratio of $\Phi = 0.745$ in an atmospheric swirl combustor. In a similar experimental setup, Prakash et al. [5] used a number of bandpass acoustic signal frequency filters centered at 15.9, 31.8, and 63.7 Hz as means of LBO detection and subsequent feedback into a pilot fuel injection control system. Taupin et al. [6] detected a non-acoustic low frequency mode measuring up to 15 kPa at 16 Hz near LBO in an

* Corresponding author at: School of Engineering, Queen's Buildings, The Parade, Cardiff, Wales CF24 3AA, United Kingdom.
E-mail address: RunyonJP@cardiff.ac.uk (J. Runyon).

Nomenclature			
<i>Abbreviations</i>		I_{OH^*}	mean integrated OH* chemiluminescence intensity
AFT	Adiabatic Flame Temperature	I'_{OH^*}	Instantaneous integrated OH* chemiluminescence intensity
AGSB	Atmospheric Generic Swirl Burner	L	length (mm)
ATAP	Ambient Temperature, Atmospheric Pressure Rig Conditions	\dot{m}_{air}	air mass flow rate (g/s)
BPV	Backpressure Valve	\dot{m}_{CH_4}	methane mass flow rate (g/s)
CFD	Computational Fluid Dynamics	p'	dynamic pressure measurement (kPa)
CMF	Coriolis Mass Flowmeter	ΔP	pressure drop (kPa)
CRZ	Central Recirculation Zone	P_2	combustor inlet pressure (MPa)
DPT	Dynamic Pressure Transducer	P_{therm}	thermal power (kW)
FCV	Flow Control Valve	Q_{noz}	burner exit nozzle volumetric flow rate (m ³)
GTRC	Gas Turbine Research Centre	Q_{tan}	Swirler tangential volumetric flow rate (m ³)
HPCR	High-Pressure Combustion Rig	r	radial distance from burner exit nozzle centerline (mm)
HPGSB	High-Pressure Generic Swirl Burner (Mk. I)	r_{noz}	burner exit nozzle radius (m)
HPGSB-2	High-Pressure Generic Swirl Burner (Mk. II)	r_{tan}	Swirler effective radius of tangential inlet (m)
HPOC	High-Pressure Optical Chamber	Re	Reynolds number
HRR	Heat Release Rate	S_g	geometric Swirl number
LBO	Lean Blowoff	S_L	laminar flame speed (m/s)
LPM	Lean Premixed	St	Strouhal number
ORZ	Outer Recirculation Zone	T_2	combustor inlet temperature (K)
PIV	Particle Image Velocimetry	\bar{u}	mean burner exit nozzle velocity (m/s)
PLIF	Planar Laser Induced Fluorescence	v	axial velocity component (m/s)
PSD	Power Spectral Density	y	axial distance from burner exit nozzle (mm)
PVC	Precessing Vortex Core	Φ	equivalence ratio
RSL	Rich Stability Limit	γ	ratio of specific heats
VSD	Variable Speed Drive	ρ	density (kg/m ³)
		μ	dynamic viscosity (Pa s)
		τ_{chem}	chemical time scale (s)
		τ_{flow}	flow time scale (s)
<i>Symbols</i>		<i>Subscripts</i>	
A_{noz}	burner exit nozzle area (m ²)	<i>comb</i>	combustor
A_{tan}	Swirler tangential inlet area (m ²)	<i>confine</i>	burner confinement
c	speed of sound (m/s)	<i>dump</i>	burner dump plane
D	diameter (mm)	<i>noz</i>	burner nozzle exit
f	frequency (Hz)	<i>premix</i>	premixed fuel and air
He	Helmholtz number		

atmospheric swirl burner at $\Phi = 0.63$. De Zilwa et al. [7] examined the lean extinction limit of a flame stabilized in a rounded duct expansion observing dominant frequencies of near-LBO oscillations of 3–10 Hz which were discrete from the acoustic frequencies of the tested geometry. Instead, these oscillations were related to flame extinction along the reacting shear layer and subsequent flashback resulting from reduced downstream strain. Numerical simulation has also been used to predict periodic ignition and extinction oscillations around 100 Hz for a premixed methane-air flame near blowoff [10].

Hence, both experimental and numerical studies have been used to enhance the understanding of LBO and its onset. However, detailed experimental characterization of stable, transitional, and unstable modes of near-blowoff operation in a geometrically generic swirl burner is lacking under representative conditions, particularly under preheated and pressurized combustion inlet conditions [4,11]. To this end, a high-pressure generic swirl burner (HPGSB-2) has been designed and commissioned in this study specifically for the purposes of enhancing the acoustic and optical measurements capable for fully premixed, confined swirl flames under these operating conditions.

1.1. Research aim

The aim of this work was to characterize experimentally the stable operation, onset, and occurrence of high amplitude, low frequency combustion instabilities observed under lean, fully premixed and near-

blowoff conditions in a generic swirl burner. In addition to providing a comprehensive data set for validation of computational fluid dynamics (CFD) models, this study also supports further development of tools for the prediction of the onset of near-blowoff instabilities in practical operating environments. A combination of techniques is therefore investigated based on the acoustic and optical measurements taken under both isothermal and combustion conditions with the goal of reducing near-LBO operating margins.

Isothermal air flow testing and loudspeaker swept-tone acoustic measurements were first undertaken to identify swirl flow structures as well as potential resonant and flow-driven frequencies of the HPGSB-2 and the surrounding rig. Methane-air combustion experimentation under atmospheric conditions was then conducted to evaluate stable operation in addition to LBO precursor events and LBO instabilities. These experiments were undertaken with fully premixed CH₄-air flames at thermal power of $P_{therm} = 55$ kW and ambient combustor inlet temperatures (~ 290 K). The resulting flames are studied experimentally through a combination of measurement techniques, most notably dynamic pressure, particle image velocimetry (PIV), OH* chemiluminescence, and OH planar laser induced fluorescence (PLIF). Additionally, a chemical kinetic modelling approach was undertaken to provide fundamental support for the analysis of flame characteristics in relation to LBO stability.

2. Experimental facilities and operation

2.1. 2nd Generation high-pressure generic swirl burner (HPGSB-2)

All experimental work was conducted using the 2nd generation design of a high-pressure generic swirl burner (HPGSB-2), housed within the high pressure optical chamber (HPOC) at Cardiff University's Gas Turbine Research Centre (GTRC). Further details concerning the design, capabilities, and utilization of this high-pressure combustion rig (HPCR) test facility can be found in previous works [12–17]. For this study, the rig has been reconfigured for high repeatability and fine control over fuel and air flows through the use of dedicated flow control valves (FCV) and coriolis mass flowmeters (CMF) on critical delivery lines. An Atlas Copco GA 45 variable speed drive (VSD) air compressor is coupled with a Beko Drypoint DPRA960 air dryer to lower the combustion air dew point prior to the air flow entering a 40 kW electric air preheater to raise the combustor inlet air temperature, although not employed in this work. When operating the burner in fully premixed mode, the fuel flow, delivered from multi-cylinder packs stored in a remote onsite location, was split after metering and introduced into the air stream prior to entering two diametrically-opposed inlets to the burner inlet mixing plenum. Rig pressurization is possible with the use of a backpressure valve (BPV) in the exhaust piping. A simplified schematic of the overall rig setup can be seen in Fig. 1. Note that the HPOC which houses the HPGSB-2, allowing for pressurized operation, is not shown in this figure. A sectioned detail view of the HPGSB-2 and HPOC assembly is shown in Fig. 2.

This generic swirl burner has been increased in scale from the atmospheric generic swirl burner (AGSB) extensively utilized at Cardiff University [18–21]. The HPGSB-2 differs from the 1st generation HPGSB [19,23–27] in that the combustor expansion ratio, defined here as the ratio of the combustor confinement ID to the burner exit nozzle ID, has been reduced from 3.5 to 2.5, achieved by a reduction from 140 mm to 100 mm of the fused quartz (GE 214) burner confinement tube ID while maintaining the burner exit nozzle diameter, $D_{noz} = 40$ mm. As shown in Table 1, both HPGSB and HPGSB-2 burners bridge the gap among the global contingent of atmospheric and pressurized confined swirl research burners, with ongoing work to further extend their demonstrated operational capabilities.

The HPGSB-2 allows optical access to the flame while achieving representative parameters of inlet pressure, temperature, and turbulence scales typical of a can-type industrial gas turbine combustor. The HPOC (Fig. 2h), rated for 1.6 MPa at 900 K, provides axial and radial line-of-sight to the burner through a set of quartz windows (Fig. 2f), allowing for the use of non-intrusive optical combustion diagnostics such as chemiluminescence, PLIF, and PIV. The HPGSB-2 is modular in its operation and geometry, both of which can be easily manipulated for parametric study of flow and flame phenomena, including both piloted and non-piloted liquid and gaseous fuel operation, varying levels of fuel/air premixing, variable geometric swirl number (S_g), combustor confinement length, and combustor outlet geometry. In this work, the burner was operated fully premixed, non-piloted, and with a fixed geometric swirl number of $S_g = 0.8$, calculated per Eq. (1) below [22],

$$S_g = \frac{A_{noz} \cdot r_{tan}}{A_{tan} \cdot r_{noz}} \left(\frac{Q_{tan}}{Q_{tot}} \right)^2 \quad (1)$$

where A_{noz} is the exit area of the burner exit nozzle (Fig. 2e), A_{tan} is the area of the tangential inlet, r_{tan} is the effective radius of the tangential inlet, r_{noz} is the radius of the burner exit nozzle, Q_{tan} is the tangential flow rate, and Q_{tot} is the total flow rate. The swirl component of the flow is generated through the use of radial-tangential swirler inserts (Fig. 2d) placed within the mixing plenum (Fig. 2c). Further detail of the combined swirler/exit nozzle insert geometry can be seen in Fig. 3, where a change in geometric swirl number can be achieved by varying the radial tangential inlet width (fixed at 7.5 mm for $S_g = 0.8$) between inserts

while maintaining all other insert dimensions.

In fully premixed operation, the fuel flow was split into two 0.0125 m diameter pipes and blended as a jet in crossflow into two 0.025 m diameter air pipes approximately 0.3 m before entering diametrically-opposed connections to the burner inlet plenum (Fig. 2b). The flow travels axially through the mixing plenum (Fig. 2c) into the radial-tangential swirler (Fig. 2d) and finally out through the burner exit nozzle (Fig. 2e) into the combustor. The face of the swirler within the combustor is covered by a 3-mm thick ceramic coating for thermal protection. The flow expands into a 6 mm thick cylindrical quartz confinement tube (Fig. 2g) of length $L_{comb} = 0.407$ m which directs the combustion products downstream towards an exhaust gas sampling probe and further through a reducer and approximately 0.710 m of water-cooled, 0.150 m diameter piping to the BPV, after which the exhaust stream was diluted and directed into an external exhaust stack.

The HPGSB-2 is fitted with an 18-mm OD instrumentation and pilot lance (Fig. 2a) inserted down the burner centerline, creating an annular space within the burner inlet plenum and mixing chamber. It contains seven 5 mm OD tubes, with one central tube intended for pilot fuel injection and the remaining six available for instrumentation. The open end of the lance protrudes 8.5 mm into the exit nozzle. Thus, if the exit nozzle was removed from the swirler, the open end of the lance would be in the same axial plane as the burner dump plane. This lance provides a bluff-body stabilization location within the burner exit nozzle while also allowing for temperature (T_{pilot}), static pressure (P_{pilot}), and dynamic pressure measurements to be made at this critical location. At the burner inlet plenum, where premixed fuel and air enter the burner, combustor inlet temperature (T_2) and pressure (P_2) are measured. Temperature (T_{comb}) and static pressure (P_{comb}) measurements within the combustor are made from the OD of the ceramic burner face. Pressure drop across the swirler, ΔP , was also measured. Temperature (T_3) and static pressure (P_3) are measured at the immediate exit of the cylindrical quartz confinement. Further detail of the HPCR, HPOC, and detailed design drawings of all wetted parts of the HPGSB-2 assembly can be found in [67].

2.2. Identification of HPGSB-2 operating limits

Table 2 below specifies the main rig operating condition ranges for each of the experimental cases in this work, isothermal air flow and ambient temperature, atmospheric pressure (ATAP) combustion. Note that the mean burner exit nozzle velocity, \bar{u} , is calculated by dividing the total premixed volumetric flow by the exit nozzle diameter, D_{noz} . The subsequent Reynolds number is calculated per Eq. (2) below,

$$Re = \frac{\bar{u} D_{noz} \rho_{premix}}{\mu_{premix}} \quad (2)$$

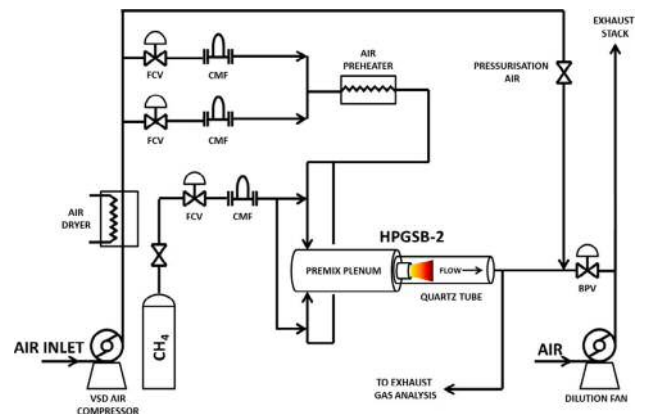


Fig. 1. Simplified schematic of the modified HPCR at the GTRC, including the HPGSB-2. Note the HPOC required for pressurized operation is not shown, see Fig. 2.

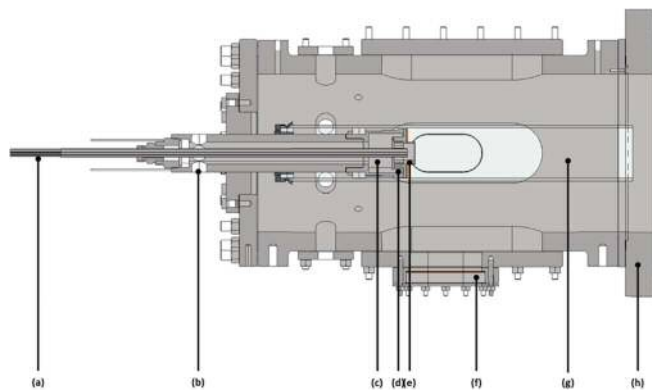


Fig. 2. Sectioned detail view of the HPGSB-2/HPOC assembly including the following critical components, (a) instrumentation and pilot lance, (b) fuel/air inlet plenum, (c) fuel/air mixing plenum, (d) radial-tangential swirler, (e) burner exit nozzle, (f) quartz optical window, (g) quartz burner confinement tube, (h) HPOC pressure casing.

where ρ_{premix} is the total premix mixture density and μ_{premix} is the total premix dynamic viscosity calculated per the Wilke correlation [68] and utilising individual component viscosities from the NIST Chemistry WebBook [69].

The burner was operated by fixing the fuel flow rate while air flow was increased or decreased to change the global equivalence ratio (Φ). The LBO stability limit was defined as the point at which the flame

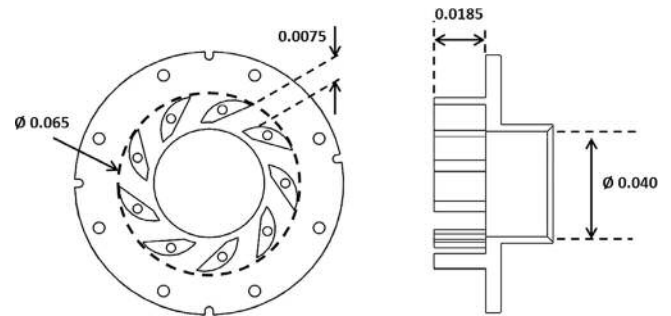


Fig. 3. Detailed geometry of radial-tangential swirler/burner nozzle insert (Fig. 2e) for $S_g = 0.8$. All dimensions in meters.

experienced high amplitude, low frequency oscillation within the rig. If possible, the burner would be driven back to a stable equivalence ratio by reducing the air flow prior to flameout. In the ATAP experimental case, the CH_4 flow rate was fixed such that $P_{therm} = 55$ kW. Under these conditions, the burner reached a rich stability limit (RSL) at $\Phi = 1.54$ where combustion could no longer be sustained within the combustor, while the LBO instability was identified at $\Phi = 0.64$. It is important to note that atmospheric pressure conditions could only be achieved by operating the HPCR with the BPV in the fully open position. Closing the BPV effectively changes the exhaust piping length, which isolates the rig from the downstream dilution fan, and consequently moderates the

Table 1
Experimental research burners for characterization of confined swirl flame stability at a range of operating pressures.

Institute	Designation	D_{dump} (mm)	$D_{confine}$ (mm)	Combustor expansion ratio	Demonstrated operating pressure (MPa)	[Ref]
Cardiff University	HPGSB-2	40	100	2.50	0.4	[67]
Cardiff University	AGSB	28	42–56	1.50–2.00	0.1	[18–21]
Lund University	Volvo VT40	54	100	1.85	0.1	[28,29]
ETH Zurich	Alstom EV5	50	94	1.88	0.1	[30,31]
Pennsylvania State University		55	110–190	2.00–3.45	0.1	[32]
MIT		38	76	2.00	0.1	[33,34]
DLR		40	85	2.13	0.1	[35]
TU-Munich	BRS Burner	40	90	2.25	0.1	[36,37]
Bucknell University		18	45	2.50	0.1	[38]
Cambridge University		37	95	2.57	0.1	[39]
NETL	ESS Burner	29.92	82.55	2.76	0.1	[40]
Korea Advanced Institute of Science and Technology		38.1	109.2	2.87	0.1	[41]
Karlsruhe Institute of Technology		–	–	2.90	0.1	[42]
Universiti Teknologi Malaysia		40	120	3.00	0.1	[43]
Georgia Tech		23	70	3.04	0.1	[2,4,5]
TU-Berlin		34	105	3.09	0.1	[44]
Lawrence Berkeley National Lab	Low Swirl Burner	57	180	3.16	0.1	[45]
EM2C		22	70	3.18	0.1	[46]
Incheon National University		40	130	3.25	0.1	[47]
Karlsruhe Institute of Technology	SBS Burner	25	89	3.56	0.1	[48]
DLR		24	89	3.71	0.1	[49]
Lund University/SINTEF	Variable Swirl Burner	15	63	4.20	0.1	[50]
King Fahd University of Petroleum and Minerals		16	70	4.38	0.1	[51]
CNRS		16	80	5.00	0.1	[6]
Sandia National Lab	CRF Burner	20	115	5.75	0.1	[52]
EM2C		25	150	6.00	0.1	[53]
Brigham Young University	ATS Burner	18	152	8.44	0.1	[54]
Cardiff University	HPGSB	40	140	3.50	0.3	[19,23–27]
EM2C	CESAM-HP Burner	30	70	2.33	0.32	[55]
Georgia Tech		19	51	2.68	0.446	[56]
Georgia Tech		19	76.5	4.03	0.446	[57]
DLR	DS Burner	40	80	2.00	0.5	[58]
CNRS		18	80	4.44	0.5	[59]
DLR	SITL DLE Burner	86	165	1.92	0.6	[60]
Pennsylvania State University		20	45	2.25	0.65	[61]
DLR	TM Burner	27.85	85	3.05	0.7	[11,62,63]
NETL	SimVal Burner	65	180	2.77	0.8	[64,65]
DLR	Twente Burner	30	85	2.83	2.0	[66]

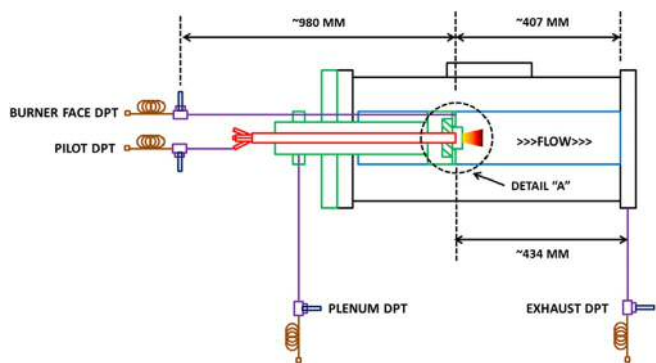


Fig. 5. Schematic of the dynamic pressure measurement system in the HPGSB-2 (green) and HPOC (black), including overall combustor length and dynamic pressure impulse line (purple) length. Note also the cylindrical quartz confinement (blue), piloted instrumentation lance (red), and 10 m semi-infinite copper tubing (brown). For Detail “A”, refer to Fig. 6. All dimensions in meters. (For interpretation of the references to colour in this figure legend, the reader is referred to the web version of this article.)

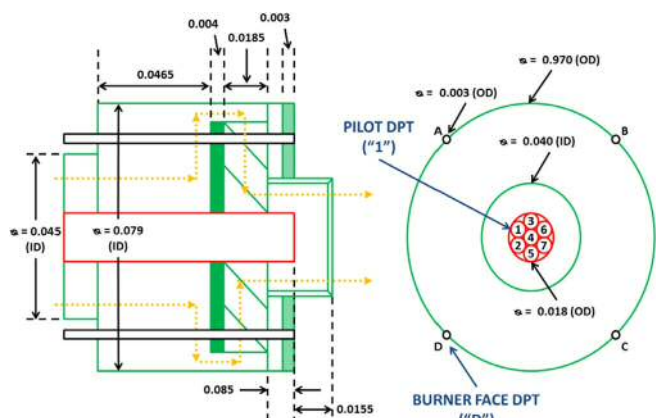


Fig. 6. Detail “A” from Fig. 5 of the HPGSB-2 (green), showing locations of the “Pilot” and “Burner Face” dynamic pressure transducers in addition to details of the instrumented pilot lance (red) bluff body location within the burner exit nozzle. Fuel/air streamlines shown in yellow. All dimensions in meters. (For interpretation of the references to colour in this figure legend, the reader is referred to the web version of this article.)

acoustic waves. The “Plenum”, “Pilot”, and “Burner Face” DPTs are PCB 113B28 with 500 kHz resonant frequency, 14.5 mV/kPa sensitivity, and 0–350 kPa range. The “Exhaust” DPT is a PCB 112A22 with 250 kHz resonant frequency, 14.5 mV/kPa sensitivity, and 0–350 kPa range. Each DPT was connected via low noise coaxial cable to a PCB 482C05 signal conditioner, and output voltages are measured via a dedicated National Instruments DAQ (PXI-6123) and processed in a bespoke NI LabVIEW program.

2.7. Chemical kinetics modelling

Chemical kinetics modelling of the experimental conditions was conducted with CHEMKIN-PRO [78] using the equilibrium tool to provide adiabatic flame temperatures (AFT) and the PREMIX program to provide laminar flame speeds (S_L) and heat release rates (HRR). The model employed the GRI-Mech 3.0 [79] reaction mechanism optimised for use with methane and natural gas compositions, comprising 53 chemical species and 325 reactions. Solutions are based on an adaptive grid of 1000 points, with mixture-averaged transport properties and trace series approximation.

3. Data processing and analytical techniques

3.1. PLIF image processing

For each stable experimental condition, 200 PLIF images were captured at a rate of 10 Hz. Instantaneous images in each data set were first corrected for background intensity and scattered light reflections imposed on the image as the laser sheet passed through the cylindrical quartz confinement tube. The laser sheet does not enter through the HPOC side window and cylindrical quartz confinement tube perpendicularly to the flow. Instead, the laser sheet was angled ($\sim 15^\circ$) to reduce the amount of reflected light imposed on the images. This is evident in Fig. 7b as the laser sheet enters from the right hand side of the image. Each image is then corrected for variations in laser sheet intensity across the sheet width using a Gaussian fit of the normalized sheet intensity values. The Gaussian fit was used to normalize the measured OH PLIF intensity values, bounding the normalization operation to the location of maximum gradient marked in Fig. 7a. The corrected instantaneous images are then temporally averaged, an example of which is shown in Fig. 7b for a stable ATAP flame ($T_2 = 293\text{ K}$, $P_2 = 0.105\text{ MPa}$, $\Phi = 0.70$) in the HPGSB-2. Note that the colormap in Fig. 7b (and for all subsequent OH PLIF images) is normalized to the maximum intensity of each image and thus does not

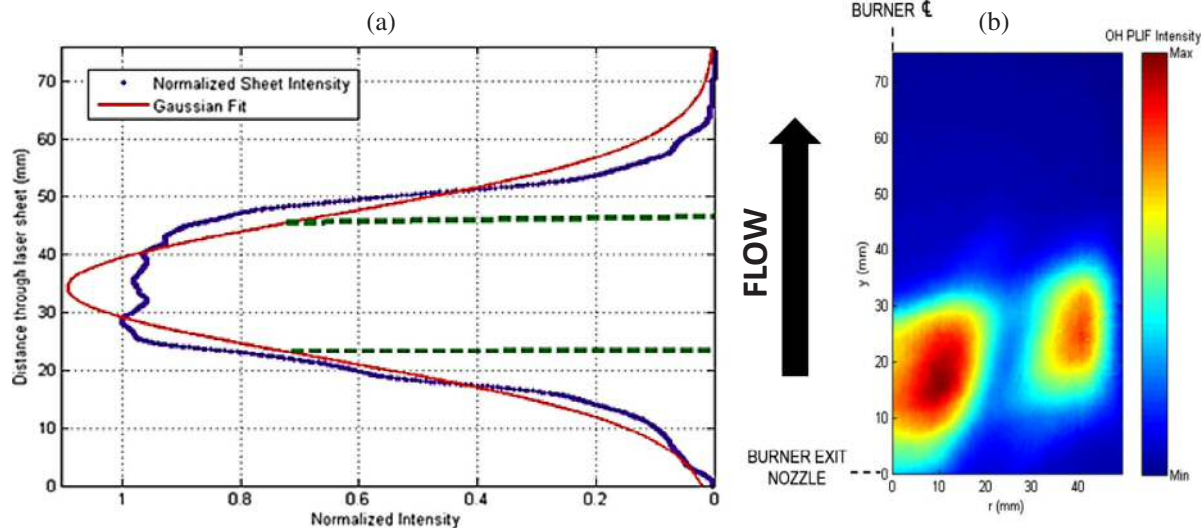


Fig. 7. Laser sheet intensity and Gaussian fit (a) used for correction of an example OH PLIF image (b) for a stable 55 kW CH_4 -air flame ($T_2 = 293\text{ K}$, $P_2 = 0.105\text{ MPa}$, $\Phi = 0.70$).

provide indication of the absolute change between images.

3.2. Chemiluminescence image processing

At each stable experimental condition, 200 images were captured at a rate of 10 Hz. At selected LBO instabilities, the chemiluminescence system was placed into a constant 10 Hz capture mode in order to observe the transition from stable operation to LBO as the global equivalence ratio was reduced. Instantaneous images in each data set were filtered using a 2-D median noise removal filter with a 3×3 pixel interrogation area. The filtered images were then temporally averaged and corrected for background intensity. A modified Abel inversion algorithm [75] was then utilized to project the line-of-sight integrated chemiluminescence intensity distribution onto a theoretical 2-D focal plane. A false colormap directly correlated to the pixel signal intensity was applied to provide visual representation of the location of the highest OH* intensity in the reaction zone, and thus indication of localised heat release. A temporally-averaged chemiluminescence image and Abel transformed image are shown for comparison in Fig. 8 for a stable ATAP flame at 55 kW ($T_2 = 293$ K, $P_2 = 0.108$ MPa, $\Phi = 0.70$) in the HPGSB-2. Note that the colormap in Fig. 8a and b (and for all subsequent OH* chemiluminescence images) are normalized to the maximum intensity of each image and thus does not provide indication of the absolute change between images.

For further comparison between OH* chemiluminescence intensity levels and heat release under varying rig operating conditions, an integral intensity (I_{OH^*}) was utilized, defined in Eq. (3) as a pixel-wise summation of the OH* intensity values from the temporally averaged and background corrected raw images, prior to Abel inversion. Instantaneous values of the filtered image integral intensity, I_{OH^*} , were also tracked throughout an image capture set to monitor the temporal variation in OH* chemiluminescence and hence heat release and flame shape.

$$I_{OH^*} = \sum_{i=1}^{1344} \sum_{j=1}^{1024} \bar{I}_{OH^*_{ij}} \quad (3)$$

As shown in Fig. 9, the integral image intensity method outlined above can be correlated to the maximum heat release rate modelled in Section 2.7 for lean ($\Phi \leq 1.00$) operating conditions which identifies a minimum OH* chemiluminescence intensity value (and HRR) that must be maintained to avoid the transition into LBO instability.

3.3. PIV image processing

At each isothermal flow condition evaluated with PIV, 200 image pairs were captured at a rate of 5 Hz. The images were first masked as the radial field of view extended outside of the quartz confinement ID.

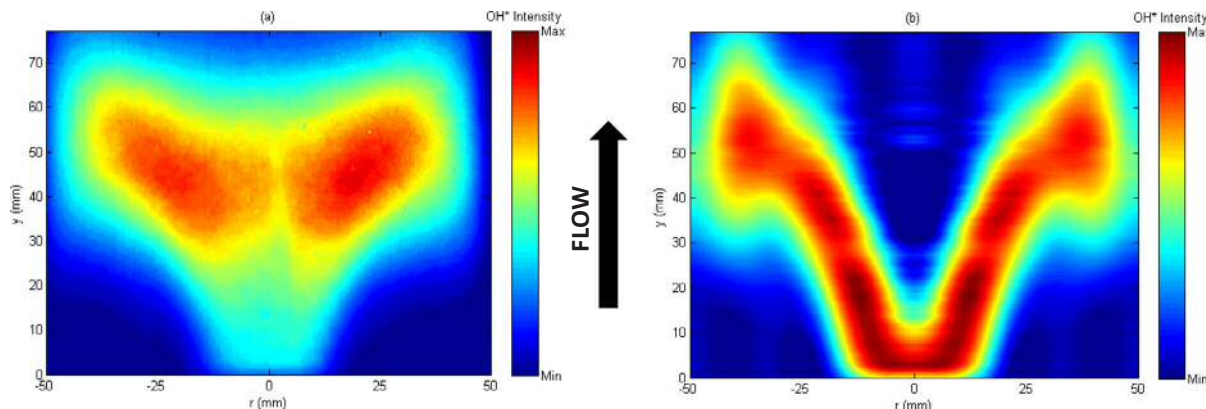


Fig. 8. Example OH* chemiluminescence image set for a stable 55 kW CH₄-air flame ($T_2 = 293$ K, $P_2 = 0.105$ MPa, $\Phi = 0.70$), comparing the (a) temporally-averaged image and (b) the equivalent Abel transformed image (b).

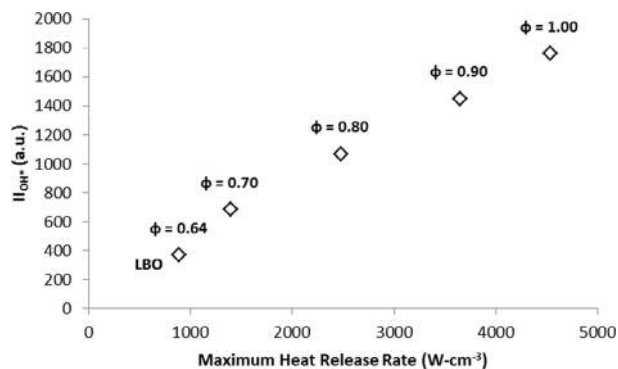


Fig. 9. Average integral intensity for OH* chemiluminescence measurements as a function of the maximum heat release rate modelled in CHEMKIN for the ATAP operating case ($0.64 \leq \Phi \leq 1$).

Then, a frame-to-frame adaptive correlation technique in Dantec's DynamicStudio was carried out to identify the two-dimensional velocity vector maps. This algorithm utilized a minimum interrogation area of 32×32 pixels (2.89 mm \times 2.89 mm) and a maximum of 64×64 (5.77 mm \times 5.77 mm), with adaptability to particle density and velocity gradients. A range validation and moving average validation were then applied to eliminate outlier velocity vectors. After this step in the image processing, the numerical files were then output and uploaded into MATLAB where bespoke processing scripts [67] were utilized to calculate a variety of flow measures such as instantaneous, fluctuating, and mean velocity components in the axial and radial direction, turbulence intensity, and integral length scale [67]. The velocity vector maps are presented with a false colormap of axial velocity contours overlaid.

3.4. Dynamic pressure signal processing

For each experimental condition plotted as a single data point, 240,000 dynamic pressure measurements were captured at a rate of 4 kHz for a total sampling time of 60 s at each of the 4 measurement locations described in Section 2.6. In addition to these fixed measurements, at selected near-LBO transitions, the DPT system was placed into a constant 4 kHz capture mode in order to resolve the transition from stable operation to LBO as the global equivalence ratio was reduced, and are consequently plotted as time-dependent values. Analysis of the time-varying dynamic pressure signals in the frequency domain provides discrete evidence of the fluctuating spectral content, amplitude, and phase. This frequency domain analysis was conducted through the use of a Fast Fourier Transform (FFT) algorithm. Normalization of the FFT output yields power spectral density (PSD). Given the 4 kHz

sampling rate utilized in this work, signal frequencies up to 2 kHz can be resolved via the Nyquist theorem, which is sufficient for resolving frequencies of interest in this work. As the LBO instability was generally observed to be less than 50 Hz, frequency filtering was incorporated where necessary, with the pressure signal filtered with a $1 \text{ Hz} < f < 100 \text{ Hz}$ bandpass filter. A dominant tone extraction algorithm was also used to discretize the dynamic pressure measurement signal into equal length parts (4000 data points) sufficient to yield the necessary frequency content information, calculating the FFT of the signal within each interval and extracting the frequency with the highest absolute amplitude.

3.5. Analytical methods

Two dimensionless analytical methods are used to quantify the experimental stability trends observed leading to prediction of the onset of the LBO instability in this burner, with the potential to extend analysis to other burner geometries subject to further study. Helmholtz (He) and Strouhal (St) number relationships have been adapted to the current burner geometry and are utilized to quantify the source of the dominant frequencies observed under isothermal flow and combustion conditions. This analysis allows for the identification of the LBO instability in the context of the natural acoustic modes and flow-driven acoustic modes of the combustor. As presented in [80] and shown in Eq. (4), the Helmholtz number provides a relationship between the dominant measured frequency and the natural acoustic mode of the combustor. It is defined by the observed dominant frequency, f , the length of the combustion chamber, L_{comb} , and the speed of sound, c , calculated based on combustor inlet conditions of T2 and $\gamma = 1.4$.

$$He = \frac{fL_{comb}}{c} \tag{4}$$

The Strouhal number, St , defined in Eq. (5) [81], provides a relationship between the dominant measured frequency and the potential instabilities arising from oscillations in the fluid flow, such as vortex shedding or a precessing vortex core (PVC). It is defined by the observed dominant frequency, f , the diameter of the burner exit nozzle, D_{noz} , and the mean burner exit velocity, \bar{u} , based on the combustor inlet conditions of total mass flow, T2, and P2.

$$St = \frac{fD_{noz}}{\bar{u}} \tag{5}$$

4. Results and discussion

4.1. Isothermal characterization

4.1.1. Isothermal acoustic characterization

Isothermal acoustic characterization of the overall combustion rig, including the HPGSB-2, HPOC, and ancillary equipment is critical to the identification of system resonant frequencies and flow-driven instabilities which could potentially influence flame stability. Prior to combustion experiments, two isothermal characterization procedures were undertaken to allow isolation of critical acoustic signatures in the rig. First, a loudspeaker was installed in the exhaust piping directly in line with the burner centreline, replacing the window which normally provides end-on radial visual access to the burner. This setup and technique are similar to those undertaken for the acoustic characterization of both industrial gas turbine combustors [82] and piping systems [83]. Using this speaker with a tone generator, a linear frequency sine sweep from 40 to 1000 Hz was conducted at a rate of 17.45 Hz/s with the rig at ambient temperature (286 K). Fig. 10 shows the temporal variation in the dynamic pressure measurement for each of the four DPTs, first with the BPV in the fully open position (Fig. 10a) and then in the fully closed position (Fig. 10b). With the BPV fully open (Fig. 10a) the burner face, pilot, and plenum DPTs exhibit amplitude spikes in the 20–40 s range of the tone sweep. Closing the BPV (Fig. 10b) has the effect of damping the higher frequency tones seen in the fully open case. Within the first 25 s of the time series, the burner face, pilot, and plenum DPTs exhibit three distinct harmonic peaks. In both cases, the exhaust DPT is shown to exhibit only a single dominant peak suggesting that this physical location exhibits a unique acoustic response compared to the other DPT locations as it is located within the HPOC casing, rather than within the burner geometry.

The frequency and magnitude spectra during the tone sweep are plotted using spectrograms of the Burner Face DPT measurement in Fig. 11, with the BPV fully open (Fig. 11a) and fully closed (Fig. 11b). With the BPV in the fully open position (Fig. 11a), the rig exhibits resonance that falls within three groups, the first near 133 Hz, the second at 280 Hz, and the third near 400 Hz. With the BPV in the fully closed

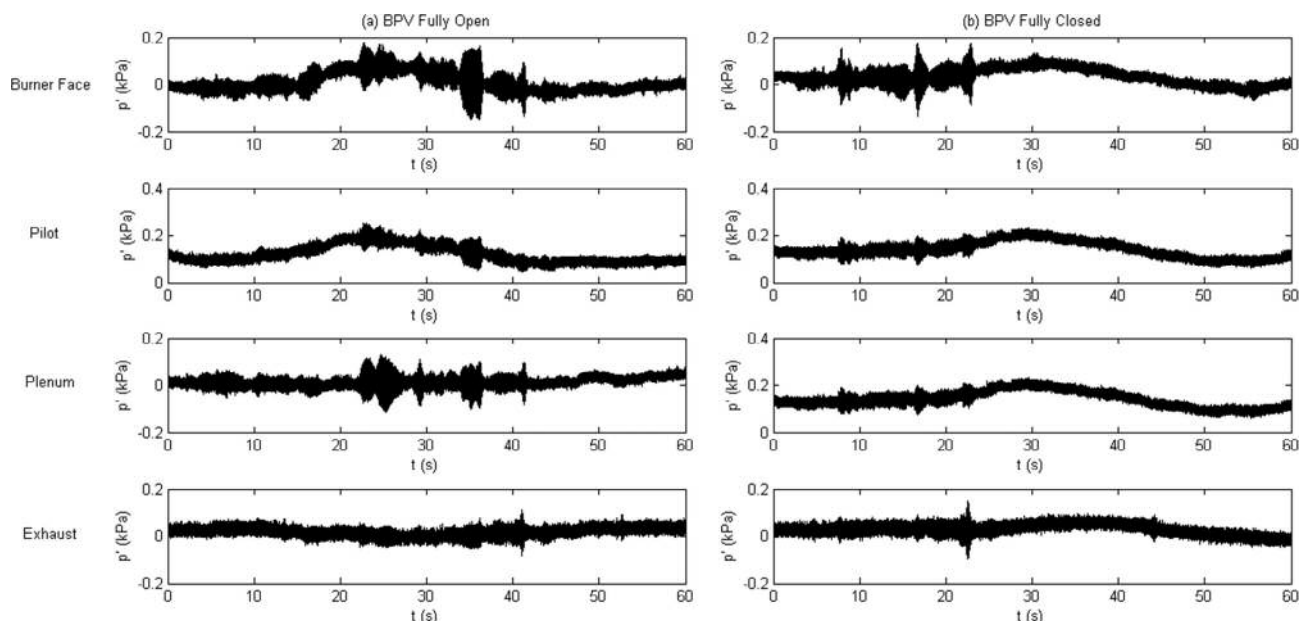


Fig. 10. Temporal variation of dynamic pressure measurement for all four DPTs during an isothermal 40–1000 Hz linear tone sweep with the BPV in the (a) fully open and (b) fully closed positions.

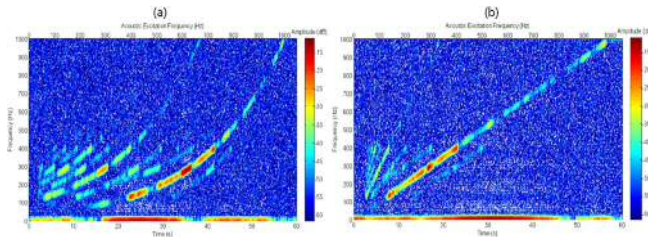


Fig. 11. Spectrograms of the Burner Face DPT measurement during an isothermal 40–1000 Hz linear tone sweep with the BPV in the fully open (a) and fully closed (b) positions.

position (Fig. 11b), the rig exhibits harmonic resonances as noted in Fig. 10b, the first near 133 Hz, the second at 292 Hz, and the third at 394 Hz. The three resonant groups show comparable dominant frequency results between the two BPV positions, although the amplitudes of the individual dominant frequencies have been reduced as a result of the reduced harmonic frequency content with the BPV closed. While the individual dominant frequencies discussed here exhibit reduced amplitudes with the BPV closed, the total pressure amplitude of the signal over the entire acoustic excitation spectrum increases from fully opened to fully closed due to increased reflections (with p'_{RMS} increasing from 11% at the Burner Face DPT to 40% at the Exhaust DPT).

It is interesting to note the high dominant frequency density in the 150–400 Hz range in the fully open case compared with the fully closed case. In the fully closed case, the dominant frequency correlates nearly linearly with the input 40–1000 Hz tone sweep, however, in the fully open case, the natural resonant frequencies dominate when the tone sweep passes through the harmonic frequencies of these resonances. For example, as the acoustic excitation frequency passes through 400 Hz ($t = 23$ s) in the fully open case, the measured dominant frequency is approximately 3 times less (133 Hz), corresponding to the high intensity region shown in Fig. 11a. Whereas the input of a harmonic frequency acts as an amplifier of the resonant frequency in the fully open BPV case, the effect of the resonant harmonic frequencies is diminished by acoustically isolating the system by closing the BPV.

An isothermal air flow experimental program was also conducted to provide baseline acoustic characteristics of flow through the HPGSB-2. Nine separate isothermal air flow conditions were investigated, a combination of air flow rates at three combustor inlet temperatures, $T_2 = 286$ K, 423 K, and 573 K, and three combustor inlet pressures, $P_2 = 0.1$ MPa, 0.2 MPa, and 0.4 MPa. For each data set of constant T_2 , the air flow rate was increased by a factor equal to the increase in P_2 , maintaining a constant $(\dot{m}_{air}\sqrt{T_2})/P_2$, and thus an approximately constant mean burner exit nozzle velocity, \bar{u} . Using the dominant frequency, the resulting Strouhal number and Helmholtz number for all experimental cases are calculated and plotted as a function of the measured frequency in Fig. 12. Note first that all measured dominant frequencies fall in the mid-frequency range given in Section 1. It is also apparent from Fig. 12 that the burner exhibits a constant $St = 0.8$ across all tested conditions of temperature and pressure, while He is shown to vary linearly with the three unique groupings identified by constant T_2 , increasing from left to right. The constant Strouhal number is indicative of a dominant frequency suggested to correspond to vortex shedding from the shear layer as the swirling flow exits the burner nozzle [80]. The dominant frequencies are thus found to collapse along a single line, dependent only on burner exit nozzle velocity, \bar{u} . PVC frequencies have also been shown to increase quasi-linearly with flow rate, thus the existence of this swirl flow instability cannot necessarily be excluded [81].

Further support that the measured dominant frequency is the result of a vortex shedding phenomena is provided in Fig. 13, where the measured Helmholtz numbers is plotted as a function of the air flow Reynolds number, calculated in Eq. (2). For a fixed T_2 and P_2 , the Helmholtz number is shown to vary linearly with Reynolds number,

which has also been shown to be indicative of vortex shedding in other work [80].

4.1.2. Isothermal flow field characterization

In addition to acoustic characterization of the HPGSB-2 and HPCR, isothermal air flow PIV measurements were conducted to provide evidence of the instantaneous and mean flow coherent structures developed in the HPGSB-2 when operated with the $S_g = 0.8$ swirler insert. Fig. 14 provides both the time-averaged mean flow field (Fig. 14a) over the entire field of view along with selected instantaneous flow field images (Fig. 14b–d) which focus on the right half of the burner only from the centerline to the confinement ID ($0 < r < 50$ mm). These images show both the total flow velocity vectors and colored contours of the axial velocity component, v . Note that the burner exit nozzle has been included (in grey) in these figures for reference. These PIV measurements were taken at $P_2 = 0.11$ MPa, $T_2 = 573$ K, and $\dot{m}_{air} = 26$ g/s, resulting in a bulk burner exit nozzle velocity of $\bar{u} = 31$ m/s. In Fig. 14a, a number of coherent flow structures typical of confined swirl flames [1,81] are visible, including a central recirculation zone (CRZ) along the burner central axis (with upstream axial flow velocities up to -17 m/s) and two radially symmetric outer recirculation zones (ORZ) at $r = \pm 40$ mm, $y = 20$ mm resulting from the flow expansion from the burner exit nozzle. Separating these two coherent structures, an outward-expanding positive axial flow and two shear layers of near-zero axial velocity are also observed. The instantaneous flow field images (Fig. 14b–d) show additional coherent structures in the flow field which are not visible in the mean images, most notably the evidence of vortices (identified by red hashed lines) shed from the burner exit nozzle along both outward expanding shear layers. These vortices are observed to wrinkle each of the shear layers between the forward flow, CRZ, and ORZ. While this observation provides support for the development of the suggested vortex shedding Strouhal number in Section 4.1.2, it must be noted that the 5 Hz repetition rate of the PIV system limits the complete resolution of the vortex shedding frequency or discretization of a PVC. While only a single isothermal condition is presented here to illustrate key flow structures, further PIV datasets for the HPGSB-2, including at elevated ambient pressure conditions and varying burner confinement geometry, are available in [67].

4.2. Ambient temperature, atmospheric pressure (ATAP) results

ATAP combustion experimentation in the HPGSB-2 was conducted at a fixed methane flow rate of $\dot{m}_{CH_4} = 1.1$ g/s, yielding $P_{therm} = 55$ kW. As shown in Table 2, the HPGSB-2 could be operated over a wide equivalence ratio range under these conditions. For the results presented, focus has been placed on lean ($\Phi \leq 1.00$) operating conditions, particularly the high-amplitude, low frequency LBO instability observed at $\Phi = 0.64$.

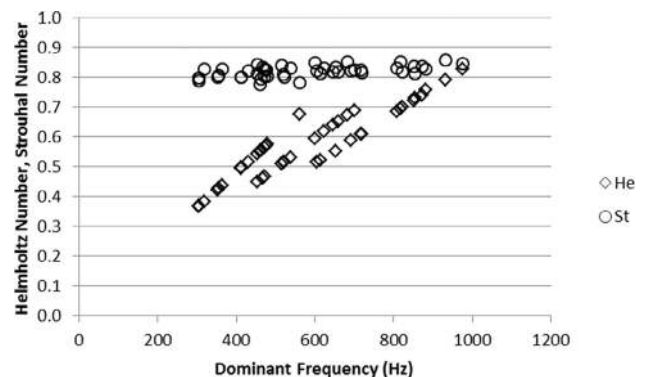


Fig. 12. Isothermal air flow Helmholtz and Strouhal numbers as a function of measured dominant frequency for $T_2 = 286$ K, 423 K, and 523 K and $P_2 = 0.1$ MPa, 0.2 MPa, and 0.4 MPa.

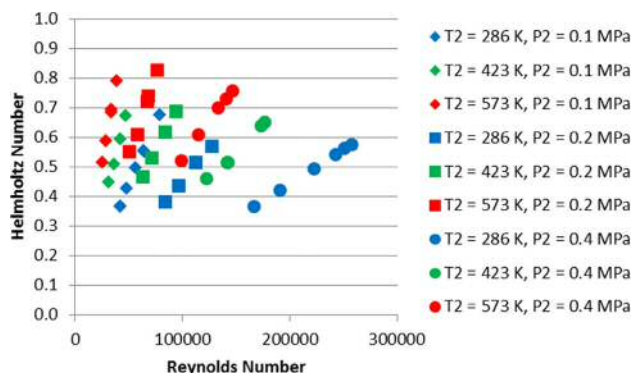


Fig. 13. Helmholtz number as a function of Reynolds number for fixed T2 and P2 isothermal air flow tests.

Abel transformed OH* chemiluminescence results are presented in Fig. 15 for three selected equivalence ratios, $\Phi = 0.64$ (Fig. 15a), $\Phi = 0.80$ (Fig. 15b), and $\Phi = 1.00$ (Fig. 15c). The image shown in Fig. 15a has been calculated using an image set of 200 images immediately prior to the onset of the observed LBO instability, defined as the first instantaneous OH* chemiluminescence image which exhibited complete flame extinction. It is evident that the heat release zones have shifted downstream as the equivalence ratio is decreased, influenced by increased \bar{u} and reduced flame speed. In Fig. 15b and c, the areas of maximum heat release are shown to lie along the outward expanding shear layer between the ORZ and CRZ observed in other work [25], yielding a V-shape flame structure which extends into the burner exit nozzle. Downstream motion of the maximum heat release region is first evident between Fig. 15c and b as the equivalence ratio is reduced, first

stabilizing approximately 40 mm downstream of the burner exit nozzle and then 50 mm downstream, while also extending in length along the shear layer. As LBO is approached (from right to left in Fig. 15), the area of maximum heat release has transitioned further downstream, and while still partially stabilized along the shear layer, increased influence of the quartz confinement tube and interaction with the ORZ is evident, causing transition to an M-shape flame. Visually the flame was observed to fluctuate in attachment to the lip of the burner exit nozzle under these near-LBO conditions. Similar fluctuations near LBO in the location of the flame stabilization location and flame root were observed by Stöhr et al. [84].

Combined RMS and temporally-averaged OH PLIF results are shown in Fig. 16 for selected equivalence ratios, $\Phi = 0.64$ (Fig. 16a), $\Phi = 0.70$ (Fig. 16b), and $\Phi = 0.80$ (Fig. 16c). The RMS OH PLIF intensity values are shown on the left hand side of each image, formulated from the instantaneous, background corrected images. The mean OH PLIF images, shown on the right of each figure, are formulated using the approach given in Section 3.1. At the approach to onset of the LBO instability, Fig. 16a, the mean OH PLIF intensity is high in the CRZ and ORZ, while the shear layer between these two zones does not appear to show any OH production. As the equivalence ratio is increased, Fig. 16b and c, the mean flame is seen to stabilize along the outward expanding shear layer, with consequently reduced OH PLIF intensity in the CRZ and ORZ compared with Fig. 16a, although some OH radicals are noted to exist in the ORZ in the $\Phi = 0.70$ (Fig. 16b) case. This observation is supported by the combined effects of reduced \bar{u} and increased S_L with increasing equivalence ratio, allowing the reaction to proceed on reduced chemical time scales and increased flow time scales (thus, further upstream towards the burner exit nozzle) compared to the near-LBO condition. This shift in flame stabilization location approaching the LBO instability is in agreement with that shown by

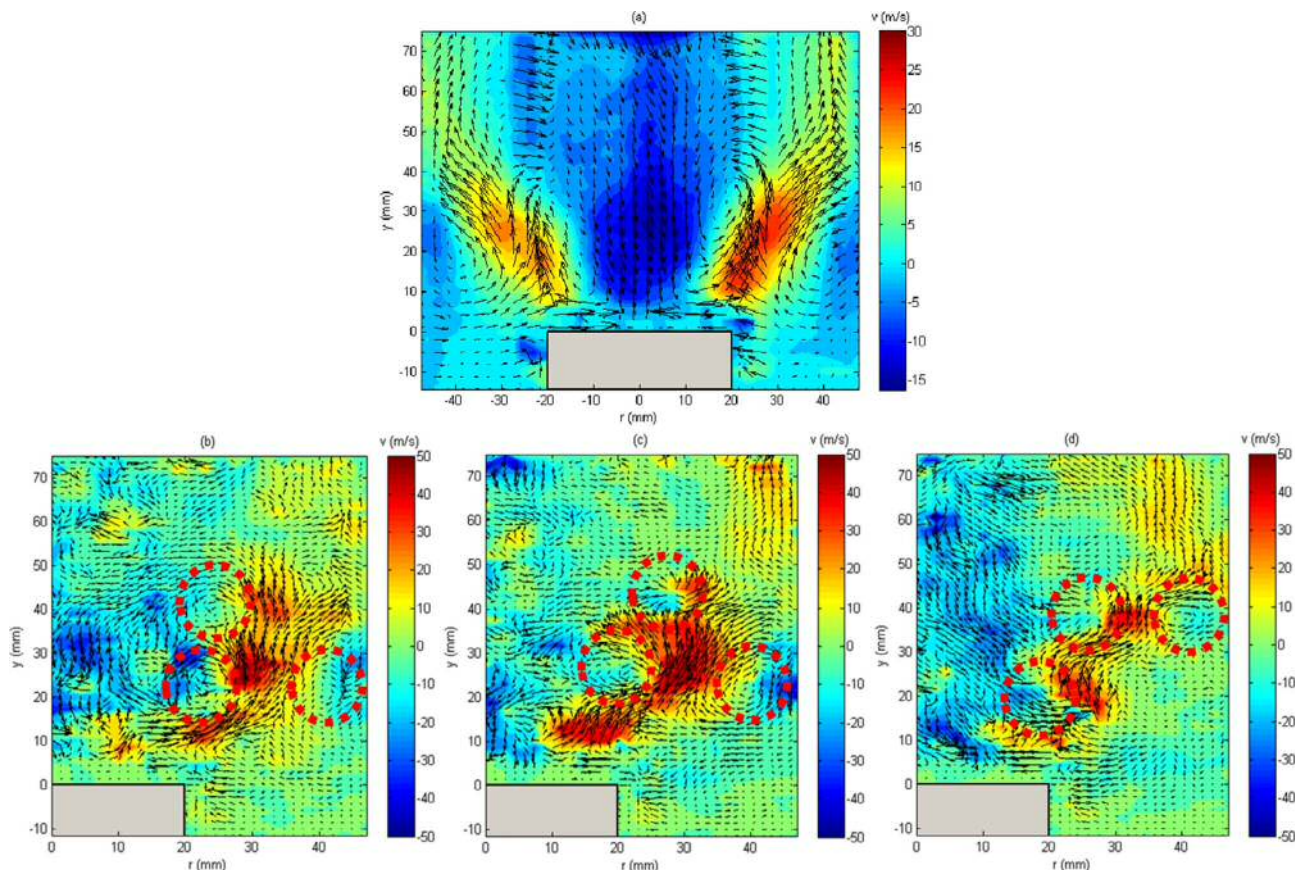


Fig. 14. Time-averaged (a) and instantaneous (b–d) isothermal PIV images including velocity vectors and colored contours of axial velocity with vortices marked in red-dashed lines. Note difference in colormap scaling. (For interpretation of the references to colour in this figure legend, the reader is referred to the web version of this article.)

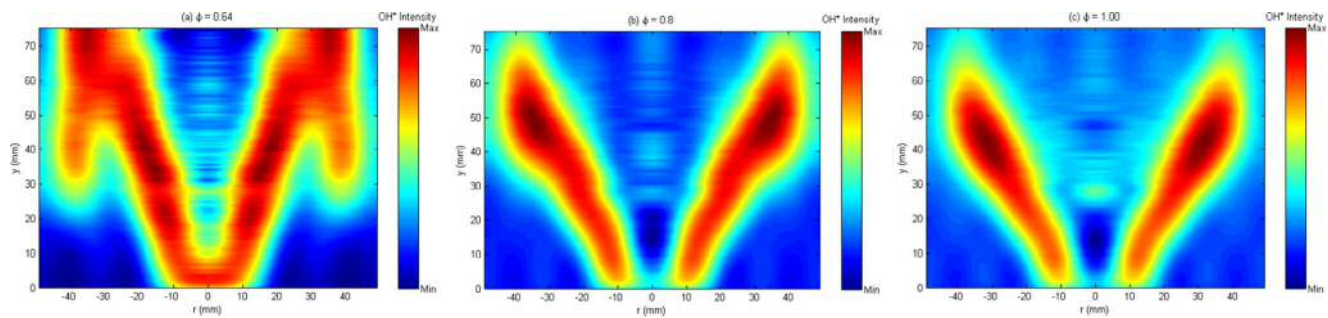


Fig. 15. Abel transformed OH* chemiluminescence images for ATAP CH₄-air flames at $\Phi = 0.64$ (a), $\Phi = 0.80$ (b), and $\Phi = 1.00$ (c).

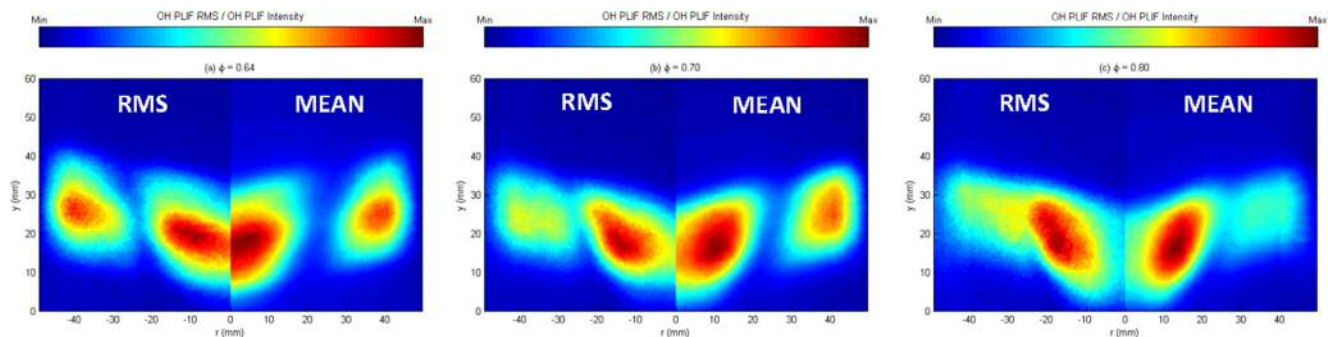


Fig. 16. Combined RMS (left) and time-averaged (right) OH PLIF images for ATAP CH₄-air flames at $\Phi = 0.64$ (a), $\Phi = 0.70$ (b), and $\Phi = 0.80$ (c).

movement of the zones of heat release in the OH* chemiluminescence images at corresponding equivalence ratios in Figs. 8 and 15. Kariuki et al. [85] noted a similar transition of the flame location from the outward expanding shear layer to the recirculation zone near LBO. It is also interesting to note the shift in fluctuating OH PLIF intensity for each condition. While the RMS values of OH PLIF follow the mean flame shape in general, there appears to be a unique distinction between the stable and near-LBO flames. At $\Phi = 0.80$ (Fig. 16b), the OH PLIF intensity tends to have its maximum fluctuation axially along the outer edge of the shear layer. Moving towards LBO (Fig. 16b and a), a shift in the general shape of the maximum OH PLIF fluctuation can be observed, taking on a more radial shape with increasing fluctuation in the CRZ and ORZ.

Instantaneous measures of OH* chemiluminescence and dynamic pressure are also useful for potentially detecting LBO precursors [2,4,5]. In Fig. 17, instantaneous OH* chemiluminescence integral intensity is shown to reduce overall as LBO is approached from $\Phi = 1.00$ to $\Phi = 0.64$, with the $\Phi = 0.64$ time series captured just before the onset of the LBO instability. With a reduction in OH* chemiluminescence intensity, the overall heat release would be expected to reduce as well, as shown in Fig. 9, until a minimum value is reached where stable operation can no longer be maintained. However, the peak-to-peak fluctuation of OH* chemiluminescence intensity values across all equivalence ratios shows little variation, implying that under ATAP conditions, the HPGSB-2 is generally stable. Thus, while mean values of integral OH* chemiluminescence intensity may give an indication of the approach to the LBO limit, monitoring the intensity fluctuation may indicate stable operation near LBO, in agreement with others [5].

Near the LBO instability, however, only a slight decrease in equivalence ratio led to periodic flame extinction and reignition events, as shown in Fig. 18. The time series plots instantaneous OH* chemiluminescence integral intensity measurements taken over a 60 s period where the air flow rate was marginally increased, from 29.0 to 29.5 g/s, to observe the onset of LBO instability as well as the LBO instability itself. The burner operational time ($t \sim 20$ s) during the LBO instability was limited to reduce potential damage to the burner before the air flow to the burner was reduced to increase the equivalence ratio and hence

re-establish stable operation. As the equivalence ratio is marginally reduced, the OH* chemiluminescence intensity gives an indication of partial flame extinction and reignition prior to complete flameout and subsequent reignition. This combination of partial and full events, as shown in the corresponding instantaneous OH* chemiluminescence images, continues throughout the LBO instability period until the flame was restabilized. Flame roll-up due to vortex shedding from the burner exit nozzle is also observed, particularly at $t = 27.2$ s. It is also interesting to note that in order to restabilize the flame during the LBO instability period, the equivalence ratio has to be increased ($\Phi = \sim 0.70$) compared to its value at the onset of the instability, $\Phi = 0.64$. This is evidenced by the higher instantaneous OH* chemiluminescence value after the LBO instability compared to its onset; this hysteresis has been reported elsewhere [61] during periods of high-amplitude, low frequency LBO instability.

Instantaneous dynamic pressure measurements were also recorded during subsequent LBO observations to identify potential acoustic indicators of LBO onset, as seen in the pressure time series plot from the Burner Face DPT shown in Fig. 19. As the equivalence ratio reduces, the dynamic pressure signal transitions from a low amplitude noisy signal

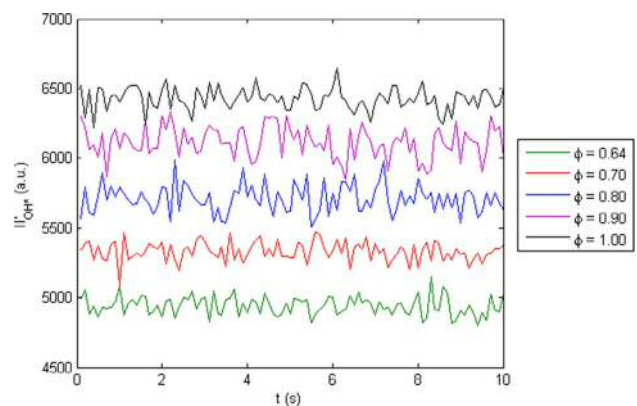


Fig. 17. Effect of equivalence ratio on the instantaneous OH* chemiluminescence integral intensity for ATAP CH₄-air flames.

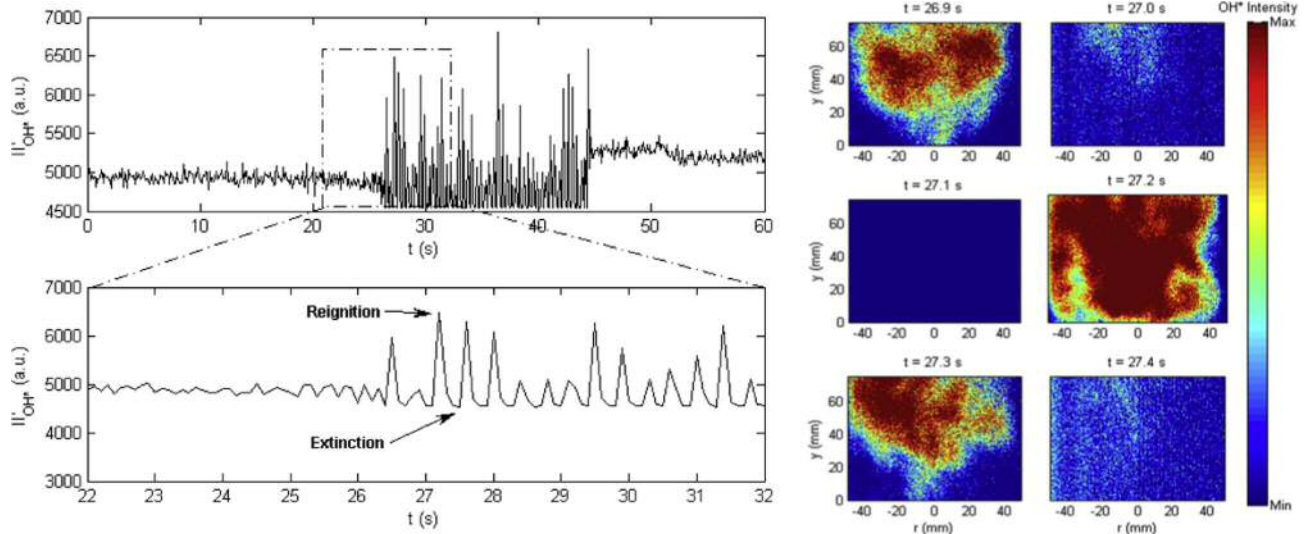


Fig. 18. Time series fluctuation of OH* chemiluminescence integral intensity (left) with selected instantaneous OH* chemiluminescence images (right) for an ATAP CH₄-air flame at $\Phi = 0.64$.

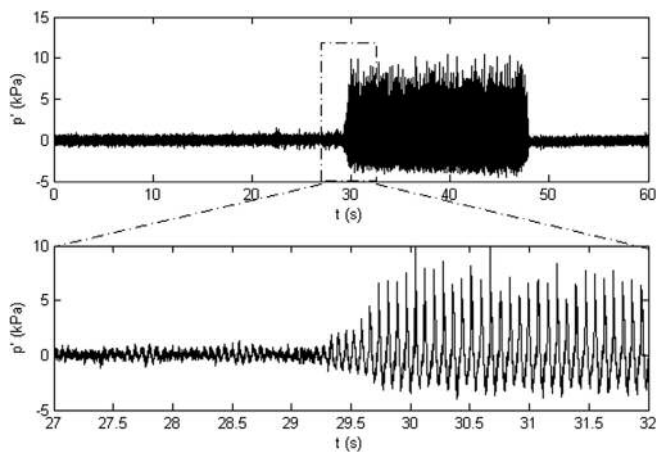


Fig. 19. Time series fluctuation in dynamic pressure measurement from Burner Face DPT (top) with inset view of LBO instability onset and limit cycle (bottom) for an ATAP CH₄-air flame at $\Phi = 0.64$.

to a high-amplitude, low frequency sinusoidal signal once the LBO instability limit cycle is established. The dominant frequency of this instability is resolved as 12–13 Hz, with a total pressure fluctuation during the LBO instability of $p'_{RMS} = 2.5$ kPa. Potential LBO indicators can be observed in the bottom time series plot at $t = 27.8$ s and 28.5 s, with distinct low amplitude sinusoidal fluctuations visible within the signal preceding the limit cycle, corresponding to partial extinction and reignition events within the combustion chamber. During the LBO instability, reignition events are captured by rapid, sharp increases in p' , whilst extinction events result in reduced dynamic pressure amplitude.

A comparison of the frequency response of all four DPTs during acoustically stable and LBO instability operation is presented in Fig. 20. For the $\Phi = 0.80$ condition, only a single dominant frequency peak of 372 Hz is observed in the Burner Face (Fig. 20e) and Pilot (Fig. 20f) DPT measurements from inside the combustion chamber and Plenum (Fig. 20g) DPT measurement at the premixed air/fuel inlet to the burner. The Exhaust DPT (Fig. 20h) also captures this 372 Hz frequency, which corresponds to a Strouhal number of $St = 0.9$, and suggests it is related to the proposed aerodynamic instability St , consistent with the isothermal analysis shown in Fig. 12. Optical diagnostic measurements under these conditions suggest stable burner operation, although instantaneous flame shape and heat release fluctuations are

still occurring, as shown in Fig. 17. This is confirmed by the DPT measurements with an average pressure fluctuation of $p'_{RMS} = 0.2$ kPa, which is an order of magnitude lower than observed during the LBO instability. However, during the LBO instability at $\Phi = 0.64$, the harmonic content at the low end of the frequency spectrum below 200 Hz is visible in the Burner Face (Fig. 20a), Pilot (Fig. 20b), Plenum (Fig. 20c) and Exhaust (Fig. 20d) DPTs, noting the change in amplitude scaling of the y-axis compared to operation at $\Phi = 0.80$.

The harmonic content of the high-amplitude, low frequency LBO instability under ATAP conditions is further evidenced when the Burner Face DPT signal is bandpass filtered ($1 \text{ Hz} < f < 100 \text{ Hz}$), as shown in the PSD plot in Fig. 21. The dominant 12.6 Hz frequency, also observed in Fig. 19, can be seen here along with its harmonics. This change in frequency distribution, from a single dominant tone under stable operation to low-frequency harmonics under LBO instability suggests that the LBO mode can be distinguished from both natural acoustic resonances of the combustion rig and potential flow-driven instabilities.

The distinctive nature of the LBO instability is supported by the variation in pressure fluctuation amplitude observed as the equivalence ratio is reduced towards $\Phi = 0.64$, shown in Fig. 22. As the equivalence ratio is reduced towards LBO, the pressure fluctuation across all four DPTs is shown to increase generally as would be expected with increased \bar{u} , despite a simultaneous collapse $\Phi = 0.70$. At $\Phi = 0.70$, the frequency spectrum of the Burner Face dynamic pressure signal is seen to be bimodal in Fig. 23, showing peaks of approximately equal amplitude at both the suggested aerodynamic instability frequency, 490 Hz ($St = 1$), and a low frequency mode at 17.4 Hz, considered a localised and partial flame extinction and reignition mode as the OH* chemiluminescence data does not indicate global flameout under these conditions. Note also the reduction in peak frequency amplitude compared to Fig. 20a and e. Once the LBO instability is established, the complete flameout and reignition events produce significant pressure pulsations in the rig, up to 2.5% of the burner inlet pressure, P2, inside of the combustion chamber.

5. Conclusions

A new generic swirl burner (HPGSB-2) has been designed and commissioned at Cardiff University's Gas Turbine Research Centre for the study of flame stability in fully premixed CH₄-air flames. In addition to extensive isothermal and stable flame characterization, a low-frequency, high-amplitude combustion instability associated with the onset of lean blowoff was identified and investigated experimentally

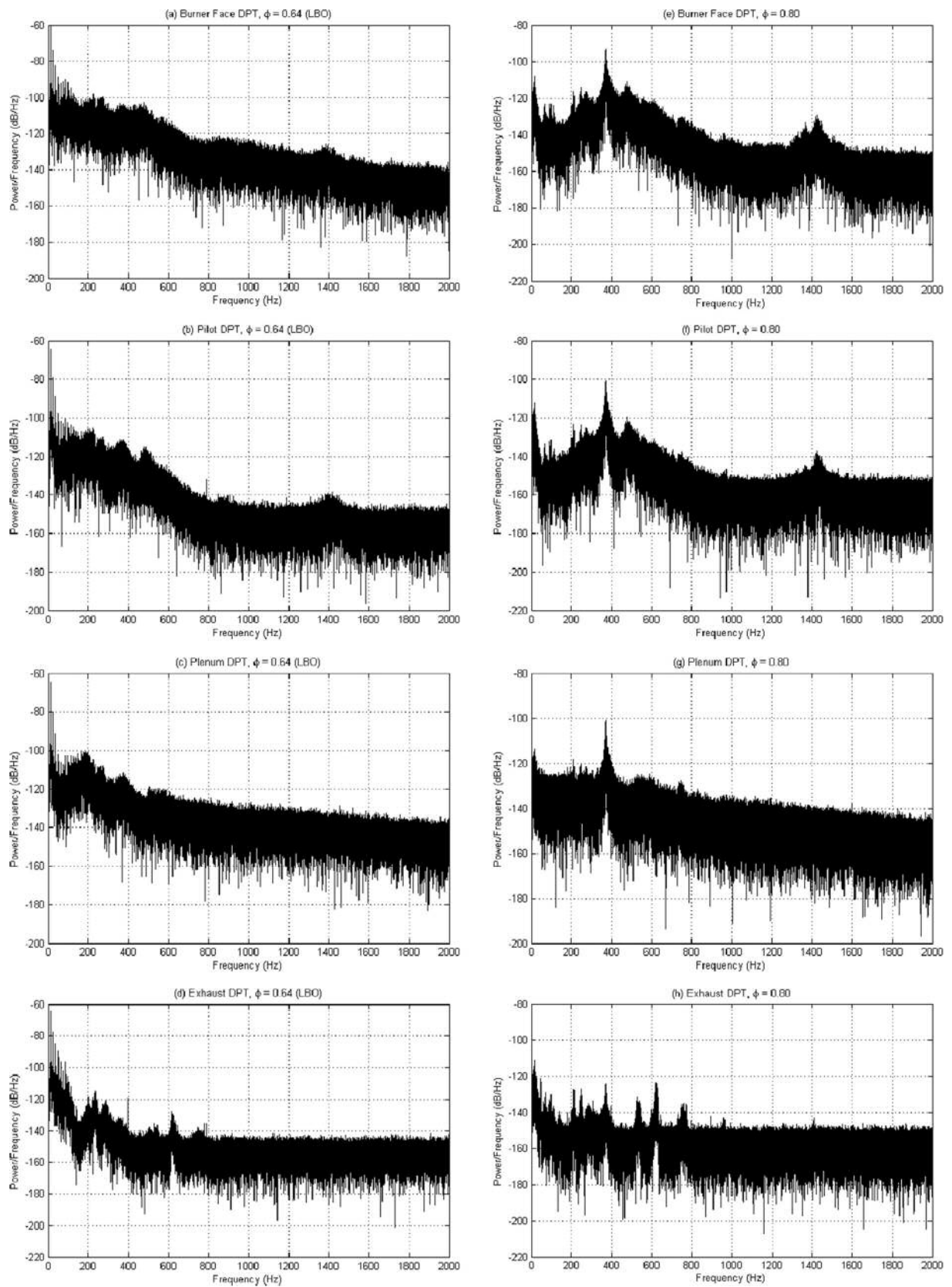


Fig. 20. PSD of dynamic pressure measurement during LBO instability at $\Phi = 0.64$ (left) and operation at $\Phi = 0.80$ (right) for each of the four DPTs, Burner Face (a, e), Pilot (b, f), Plenum (c, g), and Exhaust (d, h) for an ATAP CH_4 -air flame. Note the difference in y-axis scaling.

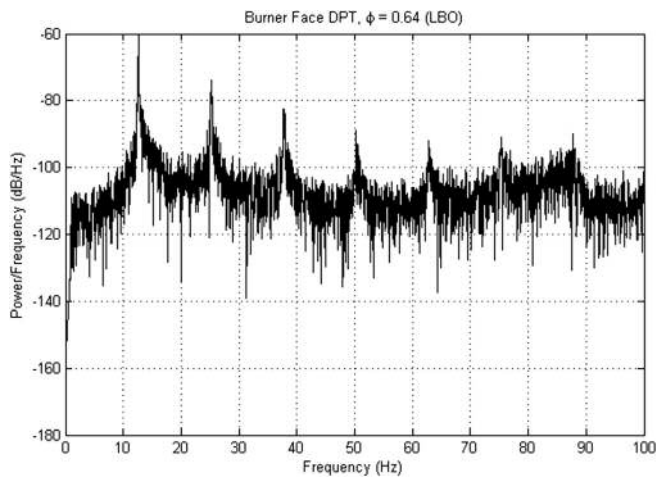


Fig. 21. Bandpass-filtered PSD for Burner Face DPT during LBO instability at $\phi = 0.64$ for an ATAP CH_4 -air flame.

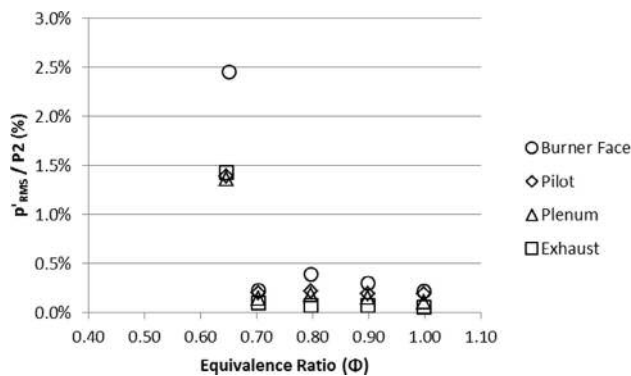


Fig. 22. Influence of equivalence ratio on the observed dynamic pressure fluctuation of all four DPTs for ATAP CH_4 -air flames.

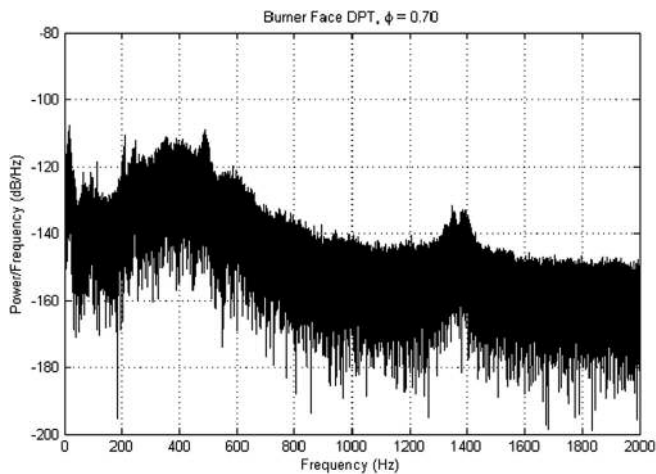


Fig. 23. PSD for Burner Face DPT at $\phi = 0.70$ for an ATAP CH_4 -air flame.

through a combination of OH^* chemiluminescence, OH PLIF, and dynamic pressure sensing techniques. This work is critical for further development of preheated and pressurized investigations of this LBO phenomenon in future work. The conclusions are:

- Extensive characterization of the combustion rig and burner through isothermal loudspeaker excitation and air flow testing in combination with Strouhal and Helmholtz number analysis facilitates the identification of natural resonant acoustic and flow-driven

instability modes. The influence of BPV position in the experimental rig is such that, under atmospheric conditions (BPV fully open), harmonic excitation of natural resonant modes appears to occur, while under pressurized conditions (BPV closed) the system does not exhibit harmonic excitation. The first acoustic mode of the burner system appears in both cases at approximately 133 Hz. Across all isothermal flow conditions, a constant Strouhal number ($St = 0.8$) as a function of dominant frequency, a linearly-varying Helmholtz number as a function of air flow Reynolds number, and instantaneous PIV images give indication of vortex shedding from the burner exit nozzle. High-speed imaging of potential aerodynamic instabilities (e.g. vortex shedding, PVC) will be the subject of future study in this burner system.

- Temporally-averaged OH^* chemiluminescence and OH PLIF imaging give indication of heat release and flame anchoring transitions from stable operation to the onset of LBO. The flame transitions from a V-shape flame attached to the instrumentation and pilot lance bluff body and stabilized along the shear layer from the burner exit nozzle to an M-shape flame which stabilizes downstream in the quartz confinement tube, with significant influence from the quartz confinement walls, CRZ and ORZs, as chemical timescales increase (e.g. reduced S_L) and flow time scales decrease (e.g. increased \bar{u}).
- Instantaneous measurements of integral OH^* chemiluminescence intensity and dynamic pressure provide evidence of the nature of the LBO instability in the context of other flow and acoustic modes. Given the relationship between OH^* chemiluminescence and the maximum heat release rate calculated from chemical kinetics modelling, there appears to be a minimum value of both HRR and chemiluminescence integral intensity at which stable operation can be maintained. The measured pressure signal is shown to collapse prior to the onset of the LBO instability, and the corresponding frequency spectra shows a bimodal system influenced by both aerodynamic instabilities and partial extinction and reignition events. Once the global equivalence ratio is further reduced to $\phi = 0.64$, periodic complete flame extinction and reignition events are observed and an acoustically-unique LBO instability is established at ~ 2 –13 Hz with observed amplitudes up to 2.5% of the combustor inlet pressure.
- The paper provides confidence in utilising the facility and associated methodologies deployed to analyse elevated ambient conditions and fuel mixtures.

Acknowledgements

This work was supported by funding from the UK Engineering and Physical Sciences Research Council through the Flexible and Efficient Power Plant: Flex-E-Plant project (EP/K021095/1). Dr. Yura Sevenco is to be acknowledged for his design and input to the development and implementation of the new swirl burner used in this work. Mr. Paul Malpas, Mr. Jack Thomas, and Mr. Terry Treherne are also thankfully acknowledged for their support in construction and installation of the burner. The experimental programme was undertaken at Cardiff University's Gas Turbine Research Centre (GTRC) in Margam, Wales, United Kingdom. Information on the data supporting the results presented here, including how to access them, can be found in the Cardiff University data catalogue at <http://doi.org/10.17035/d.2017.0011500240>.

References

- [1] Y. Huang, V. Yang, Dynamics and stability of lean-premixed swirl-stabilized combustion, *Prog. Energy Combust. Sci.* 35 (2009), <http://dx.doi.org/10.1016/j.pecs.2009.01.002>.
- [2] S. Nair, T. Lieuwen, Acoustic detection of blowout in premixed flames, *J. Propul. Power* 21 (1) (2005), <http://dx.doi.org/10.2514/1.5658>.
- [3] D. Abbott et al., The impact of natural gas composition variations on the operation of gas turbines for power generation, in: 6th International Gas Turbine Conference,

- H.C. Mongia, et al., Incorporation of combustion instability issues into design process: GE aero-derivative and aero engines experience, in: T. Lieuwen, V. Yang (Eds.), *Combustion instabilities in gas turbine engines: operational experience, fundamental mechanisms, and modeling*, Progress in Astronautics and Aeronautics, 2005, pp. 43–64, <http://dx.doi.org/10.2514/5.9781600866807.0043.0063> (Chapter 3).
- [9] J. Sewell, P. Sobieski, Combustion instability monitoring experience at Calpine, in: T. Lieuwen, V. Yang (Eds.), *Combustion instabilities in gas turbine engines: operational experience, fundamental mechanisms, and modeling*, Progress in Astronautics and Aeronautics, 2005, pp. 147–162, <http://dx.doi.org/10.2514/5.9781600866807.0147.0162> (Chapter 7).
- [10] D.G. Norton, D.G. Vlachos, Combustion characteristics and flame stability at the microscale: a CFD study of premixed methane/air mixtures, *Chem. Eng. Sci.* 58 (21) (2003), <http://dx.doi.org/10.1016/j.ces.2002.12.005>.
- [11] Y.M. Al-Abdeli, A.R. Masri, Review of laboratory swirl burners and experiments for model validation, *Exp. Therm. Fluid Sci.* 69 (2015), <http://dx.doi.org/10.1016/j.exthermfluidsci.2015.07.023>.
- [12] A. Bagdanavicius, et al., Turbulent flame structure of methane-hydrogen mixtures at elevated temperature and pressure, *Combust. Sci. Technol.* 185 (2) (2013), <http://dx.doi.org/10.1080/00102202.2012.718005>.
- [13] S. Morris, Cardiff University Progress Report July 2013. European Turbine Network FP7 H2-IGCC Project, 2013.
- [14] J. Lewis et al., The use of CO₂ to improve stability and emissions of an IGCC combustor, *ASME Turbo Expo 2014*, vol. 4A, Dusseldorf, Germany, 2014. <http://www.10.1115/GT2014-25446>.
- [15] N. Syred et al., Preliminary results from a high pressure optical gas turbine combustor model with 3D Viewing capability, in: 53rd AIAA Aerospace Sciences Meeting, Kissimmee, Florida, 2015. <http://www.10.2514/6.2015-1655>.
- [16] Y. Sevensco et al., Integrating hypersonics into a combustion test facility with 3D viewing capability, in: 20th AIAA International Space Places and Hypersonic Systems and Technologies Conference, Glasgow, 2015. <http://www.10.2514/6.2015-3654>.
- [17] A. Bagdanavicius, et al., Stretch rate effects and flame surface densities in premixed turbulent combustion up to 1.25 MPa, *Combust. Flame* 162 (2015), <http://dx.doi.org/10.1016/j.combustflame.2015.08.007>.
- [18] A. Giles, et al., Applicability of the Peclet number approach to blow-off and flashback limits of common steelworks process gases, *Fuel* 182 (2016), <http://dx.doi.org/10.1016/j.fuel.2016.05.082>.
- [19] J. Runyon et al., Methane-oxygen flame stability in a generic premixed gas turbine Swirl combustor at varying thermal power and pressure, *ASME Turbo Expo 2015*, vol. 4B, Montreal, Canada, 2015. <http://www.10.1115/GT2015-43588>.
- [20] N. Syred, et al., Effect of inlet and outlet configurations on blow-off and flashback with premixed combustion for methane and a high hydrogen content fuel in a generic swirl burner, *Appl. Energy* 116 (2014), <http://dx.doi.org/10.1016/j.apenergy.2013.11.071>.
- [21] M. Abdulsada, et al., Effect of exhaust confinement and fuel type upon the blowoff limits and fuel switching ability of swirl combustors I, *Appl. Therm. Eng.* 48 (2012), <http://dx.doi.org/10.1016/j.applthermaleng.2012.04.042>.
- [22] N. Syred, J.M. Beér, Combustion in swirling flows: a review, *Combust. Flame* 23 (2) (1974), [http://dx.doi.org/10.1016/0010-2180\(74\)90057-1](http://dx.doi.org/10.1016/0010-2180(74)90057-1).
- [23] D. Pugh, et al., Dissociative influence of H₂O vapour/spray on lean blowoff and NOx reduction for heavily carbonaceous syngas swirling flames, *Combust. Flame* 177 (2017), <http://dx.doi.org/10.1016/j.combustflame.2016.11.010>.
- [24] H. Kurji, et al., Combustion characteristics of biodiesel saturated with pyrolysis oil for power generation in gas turbines, *Renew. Energy* 99 (2016), <http://dx.doi.org/10.1016/j.renene.2016.07.036>.
- [25] R. Marsh, et al., Premixed methane oxycombustion in nitrogen and carbon dioxide atmospheres: measurement of operating limits, flame location and emissions, *Proc. Combust. Inst.* 36 (3) (2016), <http://dx.doi.org/10.1016/j.proci.2016.06.057>.
- [26] A. Valera-Medina, et al., Ammonia-methane combustion in tangential swirl burners for gas turbine power generation, *Appl. Energy* 185 (Part 2) (2017), <http://dx.doi.org/10.1016/j.apenergy.2016.02.073>.
- [27] A. Valera-Medina, et al., Ammonia, methane, and hydrogen for gas turbines, *Energy Procedia* 75 (2015), <http://dx.doi.org/10.1016/j.egypro.2015.07.205>.
- [28] R. Orbay, et al., Swirling turbulent flows in a combustion chamber with and without heat release, *Fuel* 104 (2013), <http://dx.doi.org/10.1016/j.fuel.2012.09.023>.
- [29] Y. Wu, et al., Effect of geometrical contraction on vortex breakdown of swirling turbulent flow in a model combustor, *Fuel* 170 (2016), <http://dx.doi.org/10.1016/j.fuel.2015.12.035>.
- [30] D. Fritsche, et al., An experimental investigation of thermoacoustic instabilities in a premixed swirl-stabilized flame, *Combust. Flame* 151 (1–2) (2007), <http://dx.doi.org/10.1016/j.combustflame.2007.05.012>.
- [31] D. Fritsche, Origin and Control of Thermoacoustic Instabilities in Lean Premixed Gas Turbine Combustion, PhD Thesis, Swiss Federal Institute of Technology, Zurich, 2005, <http://dx.doi.org/10.3929/ethz-a-005124957>.
- [32] A. De Rosa, et al., The effect of confinement on the structure and dynamic response of lean-premixed, Swirl-stabilized flames, *J. Eng. Gas Turbines Power* 138 (2016), <http://dx.doi.org/10.1115/1.4031885>.
- [33] S. Taamallah, et al., Thermo-acoustic instabilities in lean premixed swirl-stabilized combustion and their link to acoustically coupled and decoupled flame macro-structures, *Proc. Combust. Inst.* 35 (2015), <http://dx.doi.org/10.1016/j.proci.2014.07.002>.
- [34] G. Kewlani, et al., Investigation into the impact of the equivalence ratio on turbulent premixed combustion using particle image velocimetry and large eddy simulation techniques: “V” and “M” flame configurations in a Swirl combustor, *Energy Fuels* 30 (4) (2016), <http://dx.doi.org/10.1021/acs.energyfuels.5b02921>.
- [35] P. Weigand, et al., Laser diagnostic study of the mechanism of a periodic combustion instability in a gas turbine model combustor, *Flow Turbul. Combust.* 75 (1) (2005), <http://dx.doi.org/10.1007/s10494-005-8585-2>.
- [36] T. Komarek, W. Polifke, Impact of Swirl fluctuations on the flame response of a perfectly premixed swirl burner, *J. Eng. Gas Turbines Power* 132 (6) (2010), <http://dx.doi.org/10.1115/1.4000127>.
- [37] L. Tay-Wo-Chong, W. Polifke, Large eddy simulation-based study of the influence of thermal boundary condition and combustor confinement on premix flame transfer functions, *J. Eng. Gas Turbines Power* 135 (2) (2013), <http://dx.doi.org/10.1115/1.4007734>.
- [38] C.J. Mordaunt, W.C. Pierce, Design and preliminary results of an atmospheric-pressure model gas turbine combustor utilizing varying CO₂ doping concentration in CH₄ to emulate biogas combustion, *Fuel* 124 (2014), <http://dx.doi.org/10.1016/j.fuel.2014.01.097>.
- [39] D.E. Cavaliere, et al., A comparison of the blow-off behaviour of a Swirl-stabilized premixed, non-premixed and spray flames, *Flow Turbul. Combust.* 91 (2) (2013), <http://dx.doi.org/10.1007/s10494-013-9470-z>.
- [40] C.R. Bedick, et al., Swirling and non-swirling diffusion flame velocity measurements in a model validation combustor, in: 8th U.S. National Combustion Meeting, Park City, Utah, 2013.
- [41] K.T. Kim, Combustion instability feedback mechanisms in a lean-premixed swirl-stabilized combustor, *Combust. Flame* 171 (2016), <http://dx.doi.org/10.1016/j.combustflame.2016.06.003>.
- [42] K.U. Schildmacher, et al., Unsteady flame and flow field interaction of a premixed model gas turbine burner, *Proc. Combust. Inst.* 31 (2) (2007), <http://dx.doi.org/10.1016/j.proci.2006.07.081>.
- [43] C.T. Chong, et al., Effect of nitrogen dilution on the lean blowout limit and emissions of premixed propane/air swirl flame, *Jurnal Teknologi* 71 (2) (2014), <http://dx.doi.org/10.11113/jt.v71.3724>.
- [44] T.G. Reichel, et al., Increasing flashback resistance in lean premixed swirl-stabilized hydrogen combustion by axial air injection, *J. Eng. Gas Turbines Power* 137 (7) (2015), <http://dx.doi.org/10.1115/1.4029119>.
- [45] P.L. Therkelsen, et al., Self-induced unstable behaviors of CH₄ and H₂/CH₄ flames in a model combustor with a low-swirl injector, *Combust. Flame* 160 (2) (2013), <http://dx.doi.org/10.1016/j.combustflame.2011.11.008>.
- [46] P. Palies, et al., Experimental study on the effect of swirler geometry and swirl number on flame describing functions, *Combust. Sci. Technol.* 183 (7) (2011), <http://dx.doi.org/10.1080/00102202.2010.538103>.
- [47] J. Park, M.C. Lee, et al., Combustion instability characteristics of H₂/CO/CH₄ syngases and synthetic natural gases in a partially-premixed gas turbine combustor: Part I Frequency and mode analysis, *Int. J. Hydrogen Energy* 41 (8) (2016), <http://dx.doi.org/10.1016/j.ijhydene.2016.02.047>.
- [48] C. Kraus, et al., Experimental investigation of combustion instabilities in lean swirl-stabilized partially-premixed flames in single- and multiple-burner setup, *Int. J. Spray Combust. Dyn.* 8 (1) (2016), <http://dx.doi.org/10.1177/1756827715627064>.
- [49] W. Meier, et al., Mixing and reaction progress in a confined swirl flame undergoing thermo-acoustic oscillations studied with laser Raman scattering, *Exp. Therm. Fluid Sci.* 73 (2016), <http://dx.doi.org/10.1016/j.exthermfluidsci.2015.09.011>.
- [50] P. Sayad, et al., Experimental investigation of the stability limits of premixed syngas-air flames at two moderate swirl numbers, *Combust. Flame* 164 (2016), <http://dx.doi.org/10.1016/j.combustflame.2015.11.026>.
- [51] E.M.A. Mokheimer, et al., Numerical study of hydrogen-enriched methane-air combustion under ultra-lean conditions, *Int. J. Energy Res.* 40 (6) (2016), <http://dx.doi.org/10.1002/er.3477>.
- [52] T.C. Williams, et al., Idealized gas turbine combustor for performance research and validation of large eddy simulations, *Rev. Sci. Instrum.* 78 (2007), <http://dx.doi.org/10.1063/1.2712936>.
- [53] D. Galley, et al., Mixing and stabilization study of a partially premixed swirling flame using laser induced fluorescence, *Combust. Flame* 158 (1) (2011), <http://dx.doi.org/10.1016/j.combustflame.2010.08.004>.
- [54] P.O. Hedman, et al., Observations of flame behavior in a laboratory-scale premixed natural gas/air gas turbine combustor from planar laser induced fluorescence measurements of OH, laser doppler anemometer velocity measurements, and coherent anti-stokes raman spectrometer temperature measurements, *J. Eng. Gas Turbines Power* 127 (4) (2004), <http://dx.doi.org/10.1115/1.1914804>.
- [55] W. Tao, et al., Indirect combustion noise contributions in a gas turbine model combustor with a choked nozzle, *Combust. Sci. Technol.* 188 (4–5) (2016), <http://dx.doi.org/10.1080/00102202.2016.1139374>.
- [56] Q. Zhang, et al., Characterization of fuel composition effects in H₂/CO/CH₄ mixtures upon lean blowout, *J. Eng. Gas Turbines Power* 129 (3) (2006), <http://dx.doi.org/10.1115/1.2718566>.
- [57] D. Noble et al., Syngas mixture composition effects upon flashback and blowout, in:

- ASME Turbo Expo 2006, vol. 1, Barcelona, Spain, 2006. <http://www.10.1115/GT2006-90470>.
- [58] I. Boxx, et al., 3 kHz PIV/OH-PLIF measurements in a gas turbine combustor at elevated pressure, *Proc. Combust. Inst.* 35 (3) (2015), <http://dx.doi.org/10.1016/j.proci.2014.06.090>.
- [59] G. Cabot, et al., Experimental study of lean premixed turbulent combustion in a scale gas turbine chamber, *Exp. Therm. Fluid Sci.* 28 (2004), <http://dx.doi.org/10.1016/j.expthermflusci.2003.12.001>.
- [60] U. Stopper, et al., Experimental study of industrial gas turbine flames including quantification of pressure influence on flow field, fuel/air premixing and flame shape, *Combust. Flame* 160 (10) (2013), <http://dx.doi.org/10.1016/j.combustflame.2013.04.005>.
- [61] J.C. Broda, et al., An experimental study of combustion dynamics of a premixed swirl injector, *Symp. (Int.) Combust.* 27 (2) (1998), [http://dx.doi.org/10.1016/S0082-0784\(98\)80027-1](http://dx.doi.org/10.1016/S0082-0784(98)80027-1).
- [62] G. Lartigue, et al., Experimental and numerical investigations of self-excited combustion oscillations in a scaled gas turbine combustor, *Appl. Therm. Eng.* 24 (11–12) (2004), <http://dx.doi.org/10.1016/j.applthermaleng.2003.10.026>.
- [63] I. Boxx, et al., Study of the mechanisms for flame stabilization in gas turbine model combustors using kHz laser diagnostics, *Exp. Fluids* 54 (5) (2013), <http://dx.doi.org/10.1007/s00348-013-1532-4>.
- [64] T. Sidwell, et al., Optically accessible pressurized research combustor for computational fluid dynamics model validation, *AIAA J.* 44 (3) (2006), <http://dx.doi.org/10.2514/1.15197>.
- [65] P.A. Strakey, et al., OH-planar fluorescence measurements of pressurized, hydrogen premixed flames in the SimVal combustor, *AIAA J.* 46 (7) (2008), <http://dx.doi.org/10.2514/1.32640>.
- [66] R. Sadanandan, et al., Investigation of the syngas flame characteristics at elevated pressures using optical and laser diagnostic methods, *Flow Turbul. Combust.* 89 (2) (2012), <http://dx.doi.org/10.1007/s10494-011-9354-z>.
- [67] J. Runyon, *Gas Turbine Fuel Flexibility: Pressurized Swirl Flame Stability, Thermoacoustics, and Emissions*, PhD Thesis, Cardiff University, 2017.
- [68] C.R. Wilke, A viscosity equation for gas mixtures, *J. Chem. Phys.* 18 (4) (1950), <http://dx.doi.org/10.1063/1.1747673>.
- [69] E.W. Lemmon et al., Thermophysical properties of fluid systems, in: P.J. Linstrom, W.G. Mallard (Eds.), *NIST Chemistry WebBook, NIST Standard Reference Database Number 69*, National Institute of Standards and Technology, Gaithersburg MD, < <http://webbook.nist.gov> > (accessed August 2, 2016).
- [70] G. Kychakoff, et al., Visualization of turbulent flame fronts with planar laser-induced fluorescence, *Science* 224 (4647) (1984), <http://dx.doi.org/10.1126/science.224.4647.382>.
- [71] F. Grisch, M. Orain, Role of planar laser-induced fluorescence in combustion research, *Aerospace Lab J.* (1) (2009).
- [72] J.G. Lee, D.A. Santavica, Experimental diagnostics for the study of combustion instabilities in lean premixed combustors, *J. Propul. Power* 19 (5) (2003), <http://dx.doi.org/10.2514/2.6191>.
- [73] M. Lauer, et al., Determination of the heat release distribution in turbulent flames by a model based correction of OH⁺ chemiluminescence, *J. Eng. Gas Turbines Power* 133 (2011), <http://dx.doi.org/10.1115/1.4004124>.
- [74] Y. Hardalupas et al., Numerical evaluation of equivalence ratio measurement using OH* and CH* chemiluminescence in premixed iso-octane/air flames, in: *Proceedings of the 3rd European Combustion Meeting*, Louvain-la-Neuve, Belgium, 2005.
- [75] J. Runyon et al., Development and commissioning of a chemiluminescence imaging system for an optically-accessible high-pressure generic swirl burner, in: *Proceedings of the 7th European Combustion Meeting*, Budapest, Hungary, 2015.
- [76] D.R. Englund, W.B. Richards, The infinite line pressure probe, *ISA Trans.* 24 (2) (1984).
- [77] D.L. Straub et al., Design considerations for remote high-speed pressure measurements of dynamic combustion phenomena, in: *45th AIAA Aerospace Sciences Meeting*, Reno, Nevada, 2007. <http://www.10.2514/6.2007-561>.
- [78] Reaction Design, CHEMKIN-PRO 15092. San Diego, California, 2009.
- [79] G.P. Smith et al., GRI-Mech 3.0, 1999. Available online: < http://www.me.berkeley.edu/gri_mech/ >.
- [80] S.R. Chakravarthy, et al., Experimental characterization of onset of acoustic instability in a nonpremixed half-dump combustor, *J. Acoustical Soc. Am.* 122 (1) (2007), <http://dx.doi.org/10.1121/1.2741374>.
- [81] N. Syred, A review of oscillation mechanisms and the role of the precessing vortex core (PVC) in swirl combustion systems, *Prog. Energy Combust. Sci.* 32 (2) (2006), <http://dx.doi.org/10.1016/j.pecs.2005.10.002>.
- [82] L. Yu, M. Cashmore, An acoustic modal analysis of a DLE combustion system, in: *ASME Turbo Expo 2008*, vol. 5 A & B, Berlin, Germany, 2008. <http://www.10.1115/GT2008-51075>.
- [83] L. Tao et al., The simulation of acoustic wave propagation within networked pipe systems development and experimental validation, in: *The 22nd International Congress on Sound and Vibration (ICSV22)*, Florence, Italy, 2015.
- [84] M. Stöhr, et al., Dynamics of lean blowout of a swirl-stabilized flame in a gas turbine model combustor, *Proc. Combust. Inst.* 33 (2011), <http://dx.doi.org/10.1016/j.proci.2010.06.103>.
- [85] J. Kariuki, et al., Heat release imaging in turbulent premixed methane-air flames close to blow-off, *Proc. Combust. Inst.* 35 (2015), <http://dx.doi.org/10.1016/j.proci.2014.05.144>.